Materials & Design 258 (2025) 114511

Contents lists available at ScienceDirect

Materials & Design

journal homepage: www.elsevier.com/locate/matdes

Additive friction stir deposition vs. friction surfacing: Comparison of friction stir-based approaches for groove repair of high strength aluminum alloys

Zina Kallien [a,c,*], Victor A. Rojas [b], Pietro Aspes [a], Adam N. Swinney [b], Trevor J. Fleck [b], J. Brian Jordon [b], Paul G. Allison [b], Benjamin Klusemann [a,c]

[a] Helmholtz-Zentrum Hereon, Institute of Material and Process Design, Solid State Materials Processing, Max-Planck-Straße 1, 21502 Geesthacht, Germany
[b] Baylor University, Point-of-Need Innovations Center, Waco, TX, 76706, USA
[c] Leuphana University Lüneburg, Institute for Production Technology and Systems, Universitätsallee 1, 21335 Lüneburg, Germany

ARTICLE INFO

Keywords:
Additive friction stir deposition
Friction surfacing
Groove repair
Defect analysis
Aluminum

ABSTRACT

Friction stir-based solid-state layer deposition techniques show considerable potential as additive manufacturing approach but also for repair applications. Researchers investigate different techniques, where the layer deposition is mainly based on friction and plastic deformation of a consumable material. The approaches differ in terms of setup and if they utilize a tool to feed the consumable material. This study presents a direct comparison of different friction-based solid-state layer deposition techniques, i.e., additive friction stir deposition (AFSD) and friction surfacing (FS), for the groove repair on the example of high strength aluminum alloys. All deposition strategies present a robust process behavior for groove repair. The AFSD deposits present a sound metallurgical bonding, whereas the FS repair presents some unbonded regions; however, this is significantly improved when hybrid friction diffusion bonding (HFDB) is applied as post-processing technique to the FS deposit. A homogeneous average grain size is obtained in the AFSD deposits, whereas FS deposits present slight variations along layer thickness. The hardness distribution shows that the heat input is higher for AFSD, indicated by larger heat-affected zones in the substrate and lower hardness in the deposited material compared to FS. Overall, both approaches can achieve a successful groove repair with process-characteristic differences.

1. Introduction

Friction stir-based solid-state layer deposition techniques operate below the materials' melting temperature and enable the deposition of a metallic material as a layer via friction and plastic deformation. These technologies have gained increasing attention as they operate at lower processing temperatures [1], avoiding major challenges of fusion-based approaches related to the high temperatures as well as material melting and solidification, for instance, strong microstructural gradients [2], hot cracking [3], porosity [4], distortion [5] or high residual stresses [6]. Two approaches that are included in many recent research works are friction surfacing (FS) [7] and additive friction stir deposition (AFSD) [8]. For the FS process, a consumable stud is positioned above the substrate and experiences a defined rotational speed as well as axial force. As a result, the rotating stud is pressed onto the substrate surface, friction occurs at the materials' interface and the tip of the stud starts to deform and plasticize. A relative translational movement between stud and substrate enables the deposition of the consumable material on the substrate as a layer. The approach of AFSD is very similar to FS; however, this process uses a hollow tool to feed the consumable material, implying higher requirements on the machine setup. This tool is positioned above the substrate at a defined gap and experiences a rotational speed. The rotating consumable material is fed through the tool and achieves contact to the substrate surface, where frictional heat is generated and plastic deformation of the consumable material occurs. The subsequent feeding of the consumable material leads to filling the small gap between substrate surface and tool with plasticized consumable material. Additional frictional heating occurs when the gap is filled and the rotating tool surface is in contact with the extruded consumable material. A relative translational movement enables the deposition of the

* Corresponding author at: Helmholtz-Zentrum Hereon, Institute of Material and Process Design, Solid State Materials Processing, Max-Planck-Straße 1, 21502 Geesthacht, Germany.
E-mail address: zina.kallien@hereon.de (Z. Kallien).

https://doi.org/10.1016/j.matdes.2025.114511
Received 27 May 2025; Received in revised form 29 July 2025; Accepted 1 August 2025

Available online 6 August 2025

consumable material on the substrate as a layer at a defined thickness, i.e., the height of the gap between tool and substrate surface.

Friction stir-based solid state layer deposition approaches are good candidates to be part of modern materials' processing cycles as they are energy efficient and sustainable. Other approaches enable the processing of powder consumable, for instance, powder bed friction stir additive manufacturing [9] or particle-based friction stir additive manufacturing [10]. Many setups presented in the literature use the processing of a stud or wire, see, for instance, Chen et al. [11], where these consumables can be produced by a recycling processes [12].

FS as well as AFSD are very well known for the fined-grained microstructure in the layer enabled by dynamic recrystallization [13,14]. Moreover, researchers reported very promising mechanical properties [15,16]. Many research studies investigated these layer deposition approaches with perspective to additive manufacturing [17]; however, these approaches also show great potential for repair applications [18]. Already in 2001, Yamashita and Fujita [19] proved the feasibility of FS to fill up grooves for stainless steel. Damodaram et al. [20] presented the successful groove repair on Inconel 718 via FS. Agiwal et al. [21,22] presented FS for 304L stainless steel being capable to deposit a coating that sealed 50 μm-wide through-cracks, achieving a leak-tight repair. For AFSD, Martin et al. [23] showed that different groove geometries can be filled via AFSD with AA6061 and they found an effective depth of 2.3 to 2.6 mm for the repair, where the groove geometry did not have a significant impact. For deeper grooves, the interface between the substrate and the deposited material did not show good bonding. A follow-up study [24] included mechanical testing, where the ultimate tensile strength exceeded the one of fusion-welded AA6061, indicating that AFSD repairs exhibit improved properties compared to repairs via fusion-based processes. Avery et al. [25] showed the successful filling of a groove via AFSD with AA7075 without observing hot cracking or microstructural defects. For the same consumable material, Griffiths et al. [26] showed AFSD being an effective approach to fill up the entire volume of through-holes and wide grooves. Another work on AA7075 repair via AFSD [27] presented the successful repair of a 1.6 mm deep groove, including an in-depth analysis of the residual stress distribution. Wang et al. [28] investigated the AFSD process with regard to the repair of 5 mm deep holes. The study analyzed the effect of pre-heating and variation of rotational speed, where the ultimate tensile strength and elongation were found to be in positive correlation with the rotational speed. Zhou et al. [29] investigated the groove repair via AFSD for AA7075 and found the groove geometry affecting the properties of the repaired structure, i.e., the authors reported that a 'stair-like' design leads to improved tensile strength.

The feasibility for repair applications as well as the advantages of friction stir-based solid-state layer deposition technologies has clearly been shown in the literature. Especially for the AFSD process, current research studies investigated the properties of repaired structures in more depth. However, there is a knowledge gap in exploring the capabilities of these processes to fill larger grooves. Additionally, a direct comparison of FS and AFSD has not been done. Even though the main principles are similar, the fact that AFSD uses a tool is accompanied by additional effects on the layer formation due to material consolidation compared to FS, which does not necessitate a non-consumable tool. A direct comparison of these technologies is crucial in order to understand and select the best approach for the respective repair, particularly considering the different machine requirements. The present study investigates the process behavior of FS and AFSD on a large groove and will provide, for the first time to the best knowledge of the authors, a direct comparison of these two approaches. The aim of this work is to compare specific FS and AFSD process characteristics in general with focus on the investigation of the resulting groove repair with the respective layer deposition approaches. The study includes FS depositions in the 'as welded' condition as well as FS deposits, which underwent post-processing via hybrid friction diffusion bonding (HFDB). The HFDB technique is a process that can be used to join two materials via diffusion bonding [30] but was also shown to successfully consolidate defects in FS structures and improve the bonding [15]. The FS repairs in the 'as welded' and post-processed, i.e., consolidated via HFDB, are compared to AFSD deposition on the same groove geometry. In addition to the comparison of the process behavior and resulting layer geometry, an in-depth defect analysis via X-Ray computed as well as microstructure and hardness investigation is performed.

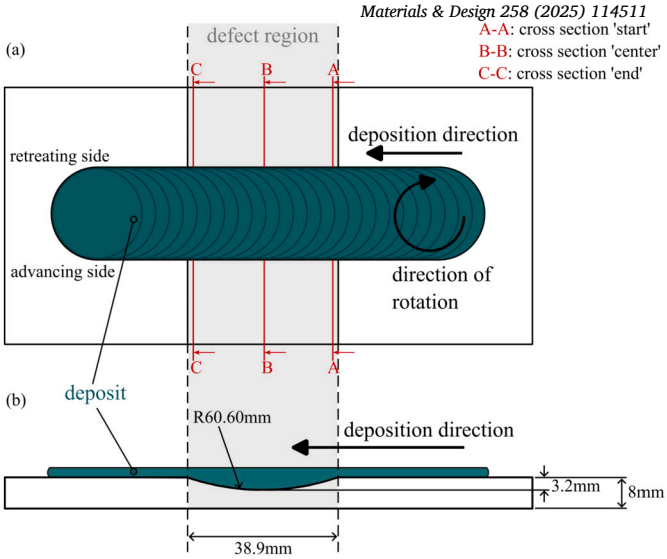

Fig. 1. Schematic of groove geometry investigated in this study and deposition strategy applied.

2. Materials and methods

In this study, different solid-state repair approaches are investigated on the example of two different high-strength aluminum alloy combinations, i.e., AA2024-T3511 deposited on AA2024-T3 and AA7075-T6 deposited on AA7475-T7531, respectively. The groove geometry[1] investigated is shown in the schematic of Fig. 1, indicating the deposition strategy, i.e., the deposition direction, for the respective single layer groove repairs. The layers were deposited across the groove to investigate and compare the behavior of the respective repair approach on the edges. Different approaches are compared, i.e., FS, FS with HFDB post-processing and AFSD, Fig. 2. The overview of the respective process parameters is given in Table 1. The details on the individual process setups as well as the investigation of the depositions are given in the following.

2.1. FS experiments

The FS experiments of this study were performed using a custom-designed friction welding system (RAS, Henry Loitz Robotik, Germany). The equipment allows to program the deposition path via computer numerical control (CNC). The process principle is presented in Fig. 2b, where the main controlling parameters are axial force, rotational speed and travel speed. The welding equipment allows for force-controlled FS layer deposition, which might be advantageous compared to feed rate-controlled FS process when grooves or uneven surfaces are the basis for the deposit. The feed rate-controlled FS layer deposition on a groove might lead to axial force differences along the deposit, which, in turn, would result in differences in terms of the deposit bonding along the deposit. In addition, force peaks, for instance, when reaching an edge during the FS layer deposition might lead to the risk of

[1] The specific groove geometry is investigated from an engineering point of view. The application scenario cannot be shared due to confidential reasons.

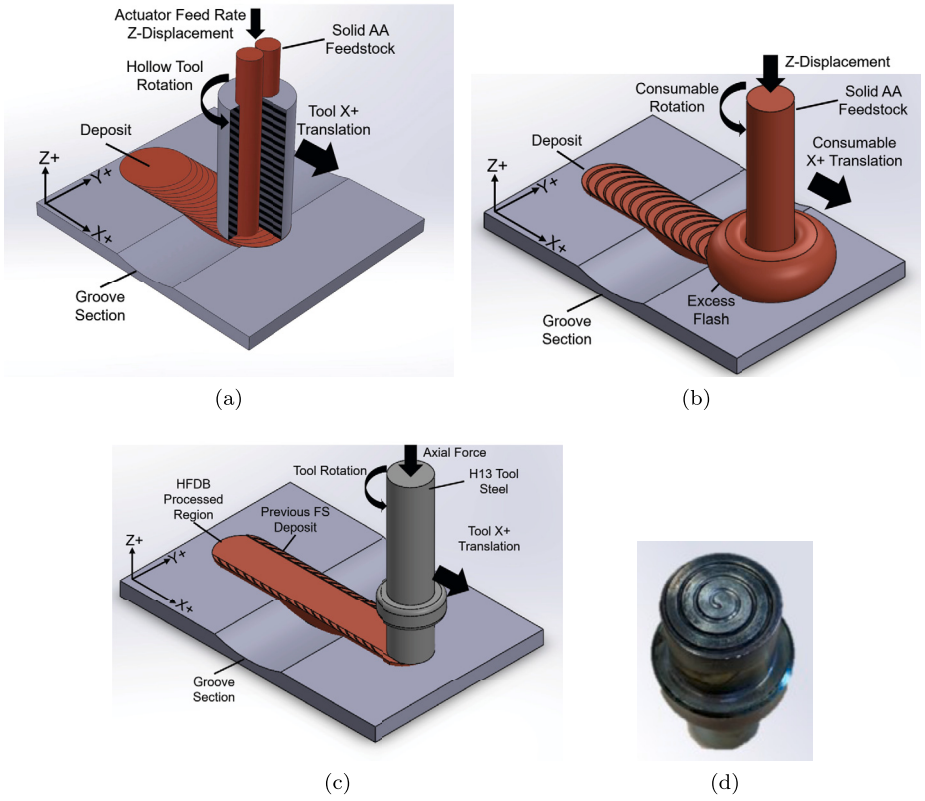

Fig. 2. The schematic of (a) additive friction stir deposition (AFSD) layer deposition process presents the setup of the tooling with two consumable rods in the AFSD tool, also known as twin rod AFSD. The main process parameters are the tool travel speed, feed rate of the consumable material and rotational speed, where the latter is driven by a temperature control. The schematic of (b) the friction surfacing (FS) layer deposition process presents the three main process parameters, which are rotational speed, axial force and travel speed. The consumable stud is used without additional tooling devices. The schematic (c) of the post-processing of an FS deposit via hybrid friction diffusion bonding (HFDB) is performed at defined tool rotational speed, travel speed and plunge depth, leading to an axial force that is applied to the subsequent structure. The HFDB tool (d) presents a convex surface with a spiral pattern.

Table 1
Overview of applied process parameters for the deposition of AA7075 and AA2024 consumable material via friction surfacing (FS) and additive friction stir deposition (AFSD) as well as parameters used for post-processing of the deposits via hybrid friction diffusion bonding (HFDB).

Alloy	Process	Axial Force [kN]	Rotational Speed [rpm]	Travel Speed [mm/s]	Feed Rate [mm/s]
AA7075	FS	8	900	1.3	0.97
	HFDB	-	1000	2.5	-
	AFSD	21	100-625	0.34375	0.21
AA2024	FS	20	600	2.5	2.10
	HFDB	-	1500	2.5	-
	AFSD	21	100-625	0.34375	0.21

stud bending, depending on the control parameters. In terms of AA2024 consumable material, the parameters were developed from a previous study by the authors [31], where AA2024 studs with 20 mm in diameter were successfully deposited. The parameters of the presented work for AA7075 are based on a study by Li et al. [32]. The travel speed was adapted in the area of the groove, i.e., the travel speed was reduced by a factor of three, to ensure that enough consumable stud material is processed to fill up the groove completely. For AA2024, the travel speed was reduced from 7.5 mm/s to 2.5 mm/s, and for AA7075 consumable material, the travel speed was reduced from 4 mm/s to 1.3 mm/s in the region of the groove, respectively. The consumable studs (23 mm diameter, 125 mm length) were deposited at room temperature. An AA2024-T351 backing plate (8 mm thickness) was added between substrate and machine table to ensure stable thermal conduction.

2.2. HFDB post-processing

The HFDB post-processing of the FS deposits was performed on the same machine (RAS, Henry Loitz Robotik, Germany) as the FS layer depositions and a schematic is presented in Fig. 2c. The non consumable HFDB tool (quenched and tempered steel X2NiCoMo18-9–5) is 22 mm in diameter and presents a slightly convex surface (0.5 mm) and a spiral groove in the contact surface. The HFDB process procedure is similar to the FS layer deposition. The rotating tool is pressed onto the surface, i.e., the FS deposit until a pre-defined plunge depth is reached. After that, a relative traveling is superimposed to the rotating tool. The process is performed in position-control and the HFDB process is repeated 5 times, where the plunge depths were ranging from 0.2 mm to 0.9 mm. For the first HFDB post-processing passes on the rough FS deposit, the plunge depth was set to lower values to achieve an even surface for the subsequent processes. The even surface allows a planar contact to the HFDB tool for subsequent processes and the plunge depth was increased step by step.

2.3. AFSD experiments

The AFSD experiments of this study were performed using an AFSD friction welding system (BOND Technologies, USA). Similar to the FS welding equipment, the deposition path is programmed via CNC, which allows free design of the path geometry. The controlling parameters for the AFSD depositions were the feed rate and the travel speed. A challenge during AFSD layer deposition at constant process parameters is the heat accumulation throughout the process, i.e., continuous temperature increase throughout the deposition, leading to different process temperatures along the deposit length [33]. This can be overcome by

using a temperature-controlled process, resulting in constant process temperatures throughout the whole layer deposition process by adapting the rotational speed [34]. Similar observations were also reported for friction stir welding and compared to AFSD [35]. In this study, a temperature control has been used, where the rotational speed is adapted within an allowed range of 100 to 625 rpm to keep a constant process temperature of 360 °C, which is measured within the AFSD tool (1 mm from tool face) using a thermocouple. The twin rod configuration has been used for this study, [36], Fig. 2a. The AFSD tool (H13 tool steel) has a diameter of 38 mm and presents a flat surface. The distance between tool face and the 8 mm thick part of the substrate was set to 0.25 mm. For each AFSD deposit, two consumable rods (12.7 mm diameter, 152.4 mm length) were used. To accommodate the twin rod depositions, the tool has two 14 mm bores that are spaced 7 mm offset from the tool center. For AFSD, there are some previous studies available in terms of groove repair by the authors. Different processing parameters for AFSD groove repairs have been used from 0.41 mm/s [37] to 0.83 mm/s [25] but these were with considerably smaller groove volumes (1-3 mm deep, 10 mm wide), so a slower speed was selected through internal trial to compensate for the extra volume that is needed to effectively fill the groove, Table 1. The process parameter set at constant travel speed presented a successful and homogeneous deposition for both consumable materials. Similar to FS, an AA2024 backing plate (8 mm thickness) was added between substrate and machine table to ensure a stable thermal conduction. Additionally, a tool preheat step prior to the deposition was implemented by adding a separate sheet of AA6061 next to the deposition plate and programming the machine to plunge, rotate and dwell until the embedded thermocouple reached 300 °C. Once the preheat temperature was reached, the tool will translate to the starting location of the deposit and initiate the deposition.

In AFSD, the support of the consumable material by a shoulder allows lower rotational speed and slower travel speed compared to FS. In FS, a higher rotational speed is necessary to keep the process stable, avoiding stud buckling. Due to the larger diameter of the AFSD tool, lower rotational speeds are necessary when the parameters should be transferred. Considering the fact that not the full consumable stud material is deposited during FS as some of the material is pushed outside, forming the FS-typical flash, the radius of the assumed contact area that actually forms the deposit is approx. 60-70% of the consumable stud radius. So, the FS rotational speeds between 600 and 900 rpm for an assumed contact radius of 6.9 mm (60% of the FS consumable stud diameter) would result in approx. 110 to 165 rpm for a 38 mm diameter AFSD tool, which is in the range of the rotational speed applied during the AFSD layer deposition by the temperature control during the experiment. The faster feeding during the FS necessitates a certain travel speed compared to the AFSD layer deposition process. In contrast, for AFSD, a slow travel speed ensures the process-characteristic 'ironing effect' of the tool shoulder on the deposit. Overall, the specific process characteristics of FS and AFSD necessitate a certain process parameter range, which presents differences. These can mainly be related to the shoulder used during AFSD and the stability that is needed to avoid consumable stud buckling during FS.

2.4. Defect analysis

X-Ray computed tomography (CT) scans were performed via a North Star Imaging (NSI) X-3000 microfocus X-Ray system (Rogers, MN, USA) across the depositions. For all scans, a voltage of 180 kV and current of 500 μA, with a focal spot size of 90 microns, was used to generate an X-Ray beam with a voxel resolution of 34 μm. After scans were complete, the deposition radiographs were analyzed using Dragonfly (Montreal, Quebec, Canada), an image segmentation software, to quantify and compare the features of interest (void content) between samples. For each dataset, three slices, or cross-sectional images, were manually classified, distinguishing between void content and material. The software then applied this classification to the remainder of the slices creating a complete mapping of the build's features (void content and material), to allow for void content analysis and imaging to compare between samples. It should be noted that the voxel size of 34 μm was used, implying that features of interest, i.e., voids, smaller than that dimension would not be identified through this approach.

2.5. Sample preparation and microscopy

Three cross sections were taken for each deposit from the start, center and end of the groove, Fig. 1. The cross sections were embedded, ground and polished following common metallographic practices. Electro-chemical etching was performed using Barker's solution at 15 V for 60 s (AA2024) and 15 V for 70 s (AA7075). Images before and after etching were taken using a light microscope (VHX-7000, Keyence, Germany). The center cross-sections were investigated using a scanning electron microscope (Thermo Fisher Scientific, USA) with an EDAX Velocity Series EBSD detector (AMETEK Inc., USA) using a voltage of 15 kV, a working distance between 15 mm and 20 mm, a magnification of × 1000, and a step size of 0.1 μm and 0.2 μm for the AA2024 and AA7075 samples, respectively. Each sample was scanned in three regions in the center along the thickness of the deposits: at the bottom of the deposit 0.3 mm away from the layer-to-substrate interface, at the top at 0.3 mm from the top edge, and at the center. The collected data was analyzed using the EDAX OIM Analysis Software, setting a minimum grain size of 10 points, and a confidence index above 0.2. The grain size was evaluated using the equivalent diameter method. The grain orientation spread (GOS) shows the average misorientation within each grain. Low GOS values are representative of a low deformed grain structure. Commonly, different threshold values are used to distinguish between refined and not refined grains [38,39]. In this work, to detect the refinement of the grain structure of the analyzed EBSD regions, a 5° threshold was set.

2.6. Mechanical properties

Hardness measurements were performed with an automated hardness testing machine (Durascan 70 G5, Emco-Test, Austria). The hardness mappings were obtained using a Vickers indenter (136° opening angle) at equidistant indent spacing of 0.5 mm at a load of 100 g with a holding time of 10 s.

A second indentation method was used to obtain data about the plastic material behavior by analyzing the profile of the indentation, following the DIN SPEC 4864 [40] standard. These tests were performed using an indentation testing machine (i3D BVR, Imprintec GmbH, Germany) for the cross-sections of all deposits taken from the center of the groove. The Type-B indenter, which has a spherical shape with a radius of 100 μm, was used to indent the sample at 5 kg. The material card "Al-unverified" was selected for the calculation of the plastic stress–strain curves. Measurements were performed within the deposit at an equidistant spacing of 2.3 mm between the indents. For more information on this testing method, the interested reader is referred to [41].

3. Results and discussion

3.1. Deposition behavior

The FS as well as the AFSD layer deposition processes presented a very robust deposition behavior on the groove. The deposits for AA2024/AA2024 and AA7075/AA7475 for all approaches investigated, i.e., FS, FS+HFDB and AFSD, are presented in Fig. 3. The FS layers present the process-characteristic rough surface appearance, Fig. 3(a, d), whereas the AFSD layers present a more homogeneous surface, resulting from the consolidation effect by the AFSD tool, Fig. 3(c, f). After HFDB post-processing, Fig. 3(b, e), the FS deposit shows a smooth surface; however, due to the dimensions of the HFDB tool that was used

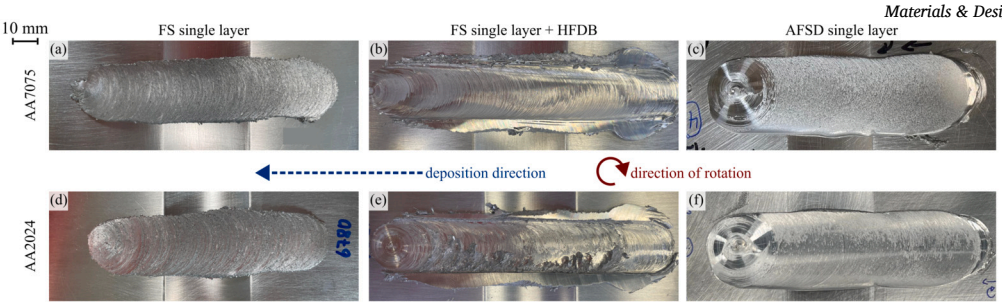

Fig. 3. Appearance of layer depositions for AA7075 consumable material for (a) friction surfacing (FS), (b) FS with hybrid friction diffusion bonding (HFDB) post-processing and (c) additive friction stir deposition (AFSD). Appearance of AA2024 deposit for (d) FS, (e) FS with HFDB post-processing and (f) AFSD. Deposition direction and direction of rotation of the deposition processes are represented by the dashed arrow and the clockwise arrow, respectively.

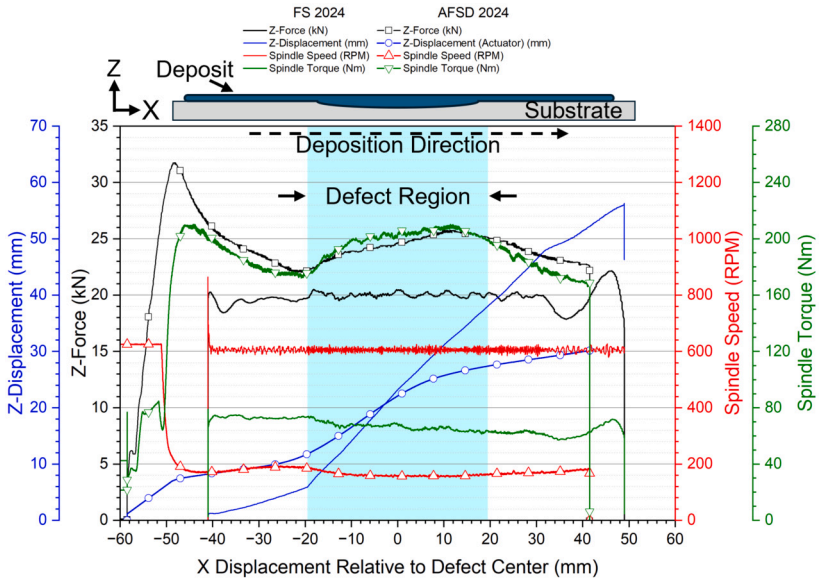

Fig. 4. Process behavior of the additive friction stir deposition (AFSD) AA2024 layer deposition and friction surfacing (FS) AA2024 consumable stud depositions relative to the groove center.

for the consolidation, a significant flash is formed at the sides of the deposit, which necessitated machining. The AFSD layers present the widest layers enabled by the 38 mm diameter AFSD tool, controlling the layer thickness, which was set to 0.25 mm.

Even though the solid-state layer deposition approaches of FS and AFSD are closely related, a direct comparison is challenging. The respective setup of the two approaches, i.e., FS using a 23 mm stud and AFSD using two 12.7 mm studs, leads to a consumable stud material cross section of 415 mm^2 (FS) and 253 mm^2 (AFSD). For FS, the force-controlled deposition process with adapted, i.e., reduced, travel speed within the groove, leads to a continuously stable feeding in axial direction, Fig. 4, with axial feed rates of approximately 0.97 mm/s (AA7075) and 2.10 mm/s (AA2024). Considering the dimensions of the consumable studs, this results in a feed volume per time of approx. 403 mm^3/s (AA7075) and 873 mm^3/s (AA2024). However, not the complete fed consumable material is forming the layer as parts of it are pushed out of the process zone, forming the FS-characteristic flash. For both alloys, the weight difference between stud before and remaining stud after the layer deposition (100 mm length) at the respective process parameters is approximately 25 g.

The AFSD process is performed in position-control, i.e., the feed rate is set to a specific value (0.21 mm/s). Considering the cross section of the AFSD consumable material, this would result in a feed volume per time of 53.2 mm^3/s. For the whole deposition process, the tool is at a fixed position above the substrate, i.e., defining the layer thickness of 0.25 mm. However, the space between tool and substrate is varying throughout the deposition process as the process travels across the groove, which leads to a gap effectively varying between 0.25 and 3.45 mm. In the start and end region, where less space is available, the resulting forces are high and reach the maximum force limit of 21 kN of the feedstock actuator which is a separate load cell from the forge forces (Z-Force), Fig. 4. When the actuator force limit is reached, the actuator modulates and reduces the feed rate via a force-control PID loop, i.e., the Z-displacement is reduced in these regions. Within the first half of the groove, the actuator force is lower and, in turn, the feed rate increases accordingly up to the prescribed speed (0.21 mm/s), resulting in an increased Z-displacement, Fig. 4. This is evident from the changing slope of the Z-displacement (actuator displacement) on Fig. 4 for the AFSD deposition, which is decreasing when the process approaches the second half of the groove region. The reduction in the actuator speed can be attributed to the feedstock experiencing increased friction within the tool as excess deposited material is accumulated along the surface, causing lateral flow to be reduced and the actuator to reach its force limit.

Overall, due to the different setups and control parameters, a direct comparison of FS and AFSD in terms of process response remains challenging. With regard to the machine setup for this specific groove repair application scenario, it can be stated that the axial forces as well as the torque are significantly higher for the AFSD setup compared to FS. The AFSD depositions were performed at a slower travel speed, resulting in a deposition process that takes longer than the one for the FS setup. A slower travel speed was used for the AFSD depositions since previous trials with faster speeds yielded depositions with under filled regions.

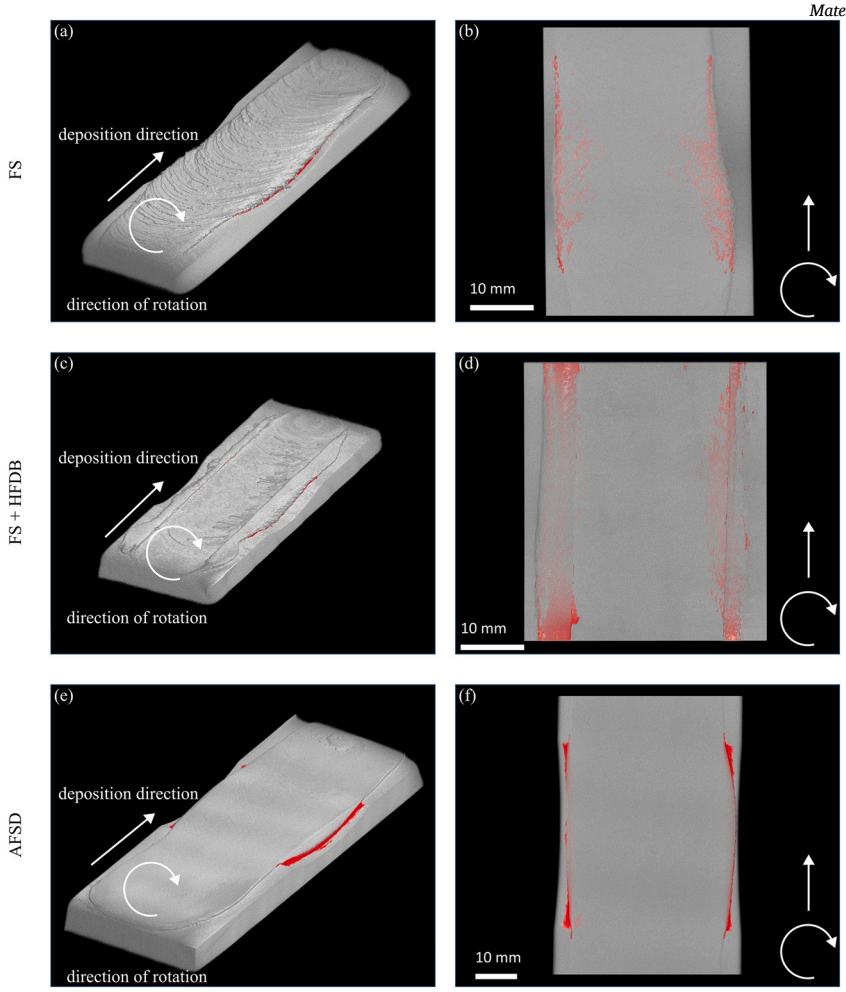

Fig. 5. X-Ray computed tomography (CT) scans for AA2024 deposited via (a-b) friction surfacing (FS), (c.-d) FS with hybrid friction diffusion bonding (FS+HFDB) post-processing and (e-f) additive friction stir deposition (AFSD). The white arrows indicate the deposition direction and direction of rotation during layer deposition. The red color indicates defect volumes of 64 μm voxel size and larger.

During the initial trials, the AFSD volumetric extrusion ratio (ratio between the amount of material extruded to the volume of space traversed by the tool during deposition) of 1.1 to 1.3 was considered based on prior experimental observations through an iterative optimization that varied traverse speed and actuator speed.

3.2. Defect analysis

The X-Ray CT investigation of the repaired grooves reveals the void volumes, where the analysis was focused on the area with the groove. The X-Ray CT images are presented in Figs. 5 and 6 for AA2024 and AA7075 consumable material, respectively. The detected voids are highlighted in red color while the deposit-substrate opacity was lowered to allow visualization through the sample.

The scans show void-free volumes in the center, where the AFSD repaired groove presents the widest void-free area, which can be related to the 38 mm width of the tool, which is discussed further in the following. For the FS sample, where no tooling was present, defects can be observed close to the center of the sample, where the void volume increases towards the center of the groove and decreases again towards the end of the groove. This can be observed for both consumable materials; however, AA7075, Fig. 6(a.2), presents significantly more void volumes, distributed in the whole groove area, than AA2024, Fig. 5(a.2).

The fact that a lower amount of defect volumes are observable for AA2024 might be related to the process parameters selected, i.e., the axial force was significantly higher for this consumable material, enabling more consolidation during FS layer deposition process.

This indicates that process optimization towards a higher axial force might lead to improvement of the layer to substrate bonding within the groove. For FS on flat surfaces, i.e., conventional sheets as substrate, the process parameters are known to affect the layer-to-substrate bonding strength [42]. However, the groove geometry might also be an influencing factor in this regard and it is necessary to perform the optimization with regard to all relevant process variables, such as specific groove, material deposition approach, etc.

The FS samples with HFDB post-processing, Figs. 5(b.2) and 6(b.2), clearly indicate the processing width of the HFDB tool. The deposit within this post-processed part presents a mostly void-free volume, i.e., reduction of defect volume compared to the respective FS deposits. The unprocessed parts of the deposits on AS and RS remain with distinct void volumes. The thermomechanical processing via HFDB, i.e., the axial force applied to the structure by the rotating tool, leads to consolidation of the FS deposited material. This observation for groove repair is similar to findings presented in terms of consolidated voids via HFDB in FS additive structures [15].

The void percentage along the layer width, i.e., from AS to RS, is presented in Fig. 7. For both consumable materials, the FS sample presents the narrowest void-free width and especially for the AA7075 consumable material, there are significant void volumes detectable close to the center of the deposit, Fig. 7b. The post-processing via HFDB clearly shows the improvement in terms of defect consolidation and resulting

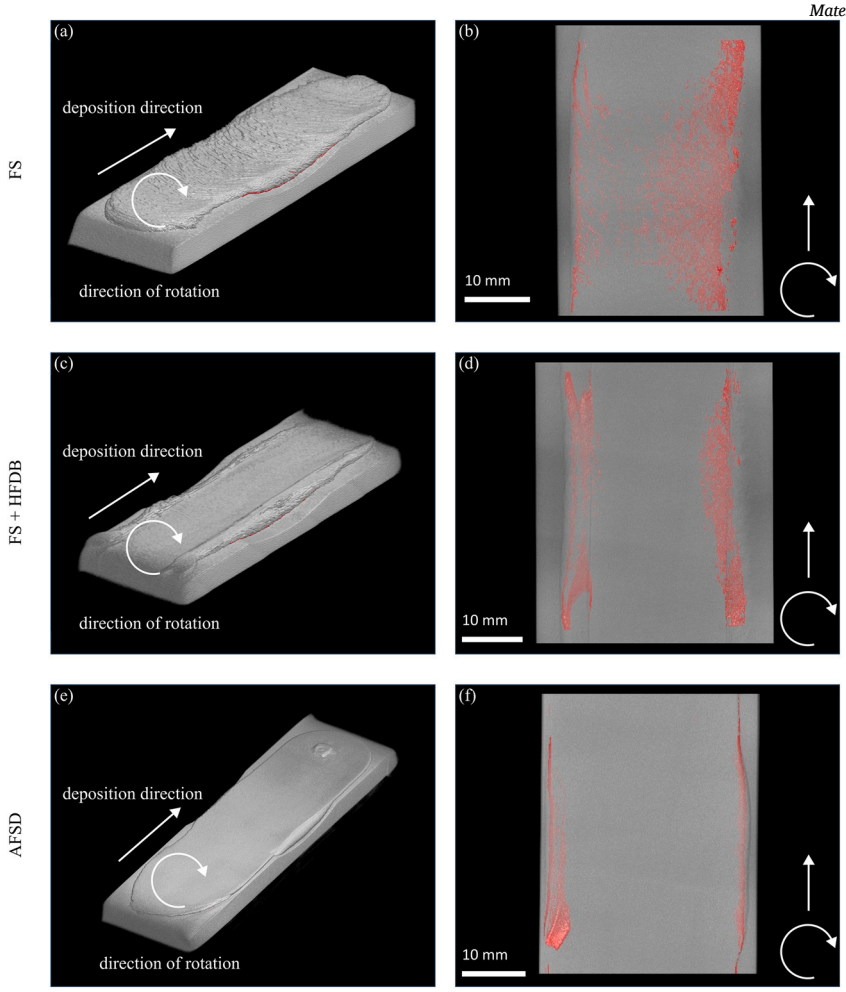

Fig. 6. X-Ray computed tomography (CT) scans for AA7075 deposited via (a-b) friction surfacing (FS), (c-d) FS with hybrid friction diffusion bonding (FS+HFDB) post-processing and (e-f) additive friction stir deposition (AFSD). The white arrows indicate the deposition direction and direction of rotation during layer deposition. The red color indicates defect volumes of 64 μm voxel size and larger.

in a wider part of the deposit that shows a very low void percentage. Especially the regions, where the FS samples present void percentages of around 1%, HFDB is capable to fully consolidate this material as long as it is within the HFDB effective processing path, which is determined by the tool diameter used. In addition, the data analysis clearly illustrates that the widest deposits at void volume below 0.5% are achievable via the AFSD approach; however, these samples present the most distinct defect volumes at the sides of the deposit. This finding is attributed to the setup, namely the tool diameter used in this study. Using a larger HFDB tool diameter for the processing of FS deposits might lead to a wider and nearly void-free width as well. This might be an interesting aspect to consider for setups for future research towards applications.

Considering the maximum width of the consumable material, it is 23 mm for FS and 25.4 mm for AFSD. However, AFSD uses a smaller consumable material cross section and less volume per time is fed, this deposition approach presents the widest layers. Considering the joining efficiency, $\eta_{joining}$, which is the ratio of the bonded part of the layer to the overall layer width, i.e., $\eta_{joining} = \frac{bonded\ width}{deposit\ width}$, the AFSD presents the highest joining efficiency, Table 2. This is in agreement with observations from the cross sections (Figs. 8-13), where the AFSD deposits present smaller unbonded edges. Especially the FS AA7075 sample presents a narrow bonded width, leading to a low joining efficiency. This is related to the voids at the layer-to-substrate interface, which will be discussed in more detail in the following section. Considering the respective tool diameters, the ratio of bonded width per tool diameter can be introduced as $\eta_{tool\ joining}$,[2] where $\eta_{tool\ joining} = \frac{bonded\ width}{tool\ diameter}$. Considering the respective tool diameter, the effectiveness of the HFDB post-processing is highlighted, presenting $\eta_{tool\ joining}$ above 80%, which is a significant improvement compared to FS and is also higher than the values obtained for AFSD, Table 2. However, high $\eta_{tool\ joining}$ can be achieved via FS for AA2024, where the samples present a large bonded

Table 2
Deposit width (measured from cross sections) and bonded width (deposit width with void percentage <0.5% obtained from X-Ray tomography) and calculated joining efficiency, $\eta_{joining}$, as well as tool joining efficiency, $\eta_{tool\ joining}$, for all deposition approaches and materials investigated.

consumable	process	deposit width [mm]	bonded width [mm]	$\eta_{joining}$ [%]	$\eta_{tool\ joining}$ [%]
AA2024	FS	29.6	20.0	67.6	87.0
	FS+HFDB	33.1	18.2	55.0	82.7
	AFSD	37.5	25.2	67.2	66.3
AA7075	FS	28.6	11.7	40.9	50.9
	FS+HFDB	33.5	17.8	53.1	80.9
	AFSD	37.3	27.7	74.3	72.9

[2] As FS does not use a tool, the stud diameter of 23 mm was taken into account for the FS samples. For the FS+HFDB and AFSD samples, 22 mm and 38 mm diameters were taken into account, being the diameters of the HFDB tool and AFSD tool, respectively.

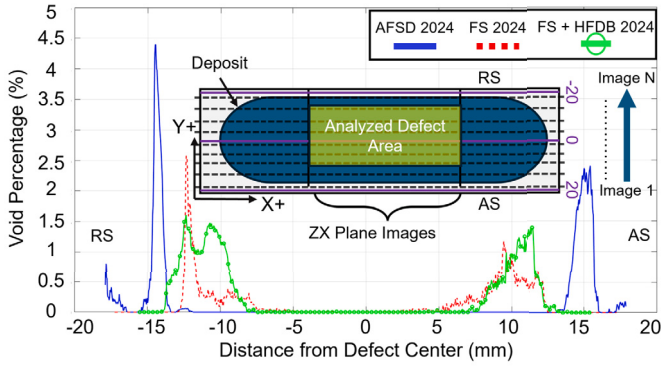

(a)

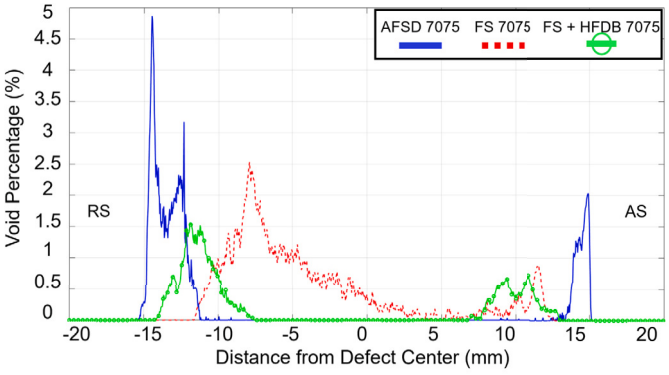

(b)

Fig. 7. Defect volume (void percentage [%]) along deposit width, i.e., from retreating side (distance from center < 0 mm) to advancing side (distance from center > 0 mm) within the groove for (a) AA2024 and (b) AA7075 consumable material. Deposits obtained via friction surfacing (FS), FS with hybrid friction diffusion bonding (FS+HFDB) and additive friction stir deposition (AFSD).

width, leading to high tool bonding efficiency when the stud diameter is considered, Table 2.

Three cross sections were taken from the repaired grooves, Fig. 1, and provide further insight in addition to the CT scans. The AA2024 FS deposit presents the FS-characteristic bonded width observable for the samples taken from the start and end, whereas the sample taken from the center of the groove exhibits voids along the whole layer-to-substrate interface, Fig. 8, which was not observable to that detail from the corresponding CT scan, Fig. 5(a). In the center of the groove, the substrate has the largest distance to the actual process zone, i.e., the tool face, and as the process advances, a transition from one edge of the groove to the other edge of the groove is occurring. These aspects lead to the assumption that achieving bonding in the center of the groove is more challenging for this deposition strategy. For the FS samples with HFDB post-processing, Fig. 9, the bonding is significantly improved, especially within the center of the groove, underlining the effectiveness of HFDB defect consolidation for FS-deposited structures, which has been proven for multi-layer FS [15]. The AFSD AA2024 sample, Fig. 10, presents a wide deposit with a very homogeneous thickness. Only the outer edges present some unbonded part, where this seems to be most distinct for the sample taken from the end of the groove. The AA7075 consumable material on the AA7475 sheet mainly shows a similar characteristic compared to the AA2024 samples. For the FS sample, Fig. 11, all three cross sections taken from the deposit present distinct defects along the layer-to-substrate interface. This is in agreement with the observations from the CT scans, Fig. 6(a). Again, the HFDB post-processing improves the bonding presented by the cross sections, Fig. 12. At the edges of the groove, i.e., for the cross sections taken from start and end, deformation of the substrate and slight mixing of substrate material into the deposit

Table 3
Fraction of grain orientation spread (GOS) values below 5° of friction surfacing (FS), FS with hybrid friction diffusion bonding (FS+HFDB), and additive friction stir deposition (AFSD) of AA2024 and AA7075 samples, for scans in the bottom, center, and top positions within the center of the groove.

	Position	AA2024			AA7075		
		FS	FS+HFDB	AFSD	FS	FS+HFDB	AFSD
GOS < 5°	top	0.982	0.987	0.958	0.971	0.960	0.973
	center	0.994	0.999	0.980	0.997	0.989	0.992
	bottom	0.991	0.999	0.976	0.991	0.993	0.991

are observable. Similar to AA2024, the AA7075 AFSD sample presents a wide deposit with a very homogeneous thickness with a small amount for deposited material forming unbonded edges, Fig. 13.

3.3. Grain size

The average grain size was analyzed at three positions in the center of the cross sections taken from the center of the groove, Fig. 14, where the number fraction grain size distribution is presented for the center scan position of the respective deposits. For the AA2024 material, the AFSD sample, Fig. 14(c.1-c.3), presents a homogeneous average grain size along layer thickness, which is known from literature [43], whereas the FS layer, Fig. 14(a.1-a.3), shows slightly coarser grains in the center than near the top and bottom, which was reported to be characteristic for FS [44] and can be related to the material flow mechanism during FS, where local temperature and strain rate gradients are present [45]. Few elongated grains can be seen in the IPF maps of the AFSD sample. The presence of elongated grains was already reported in literature in double 4 mm thick friction extrusion additive manufacturing deposit, a process very similar to AFSD [46]. It is assumed that those are non fully recrystallized grains of the feedstock material. Their number is very low, thus they do not affect the mean grain size results. Overall, the average grain size is within a comparable range for FS and AFSD, i.e., between 1.1 and 1.9 μm. The HFDB post-processing leads to additional thermo-mechanical processing cycles, resulting in larger average grain size in the respective top and center position of the deposit, Fig. 14(b.1-b.3), whereas the bottom remains similar to before. This indicates that the microstructure processing depth of the HFDB post-processing cycles is above the layer-to-substrate interface, resulting in an unaffected average grain size of the bottom part of the deposit. However, above the bottom part, HFDB is processing the fine-grained FS deposited material and leading to a grain size increase towards the top of the layer, which might be related to grain growth enabled by the HFDB process temperatures. This is a result of the additional accumulated thermo-mechanical cycles during every HFDB pass. The effect of multiple passes of a friction stir-based materials processing technique is part of some investigations available in the literature. For instance, for friction stir processing, which is a materials processing technology comparable to HFDB, El-Rayes and El-Danaf [47] also observed that multiple processing passes lead to an increased grain size. For the AA7075 deposits, the results with regard to the average grain size, Fig. 15, are in good agreement with the findings on the AA2024 samples and are not discussed in detail for brevity.

To further assess the grain refinement by dynamic recrystallization, the fraction of GOS below 5° is shown in Table 3. For all the scanned positions and samples, a value above 0.958 is reported, confirming the refinement grains via dynamic recrystallization [48].

3.4. Mechanical properties

The hardness mappings are shown in Fig. 16 for AA2024 and AA7075 consumable material, respectively. For both materials, the FS sample presents the smallest heat-affected zone. This is related to the fact that the FS sample underwent only one single thermo-mechanical processing cycle, i.e., the layer deposition process. In contrast, the approach

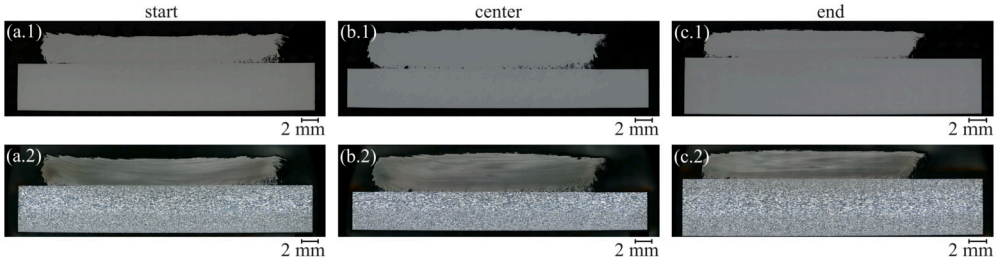

Fig. 8. Macrographs before and after etching for cross sections taken from AA2024 FS deposit at (a) start, (b) center and (c) end along the groove, as presented in Fig. 1.

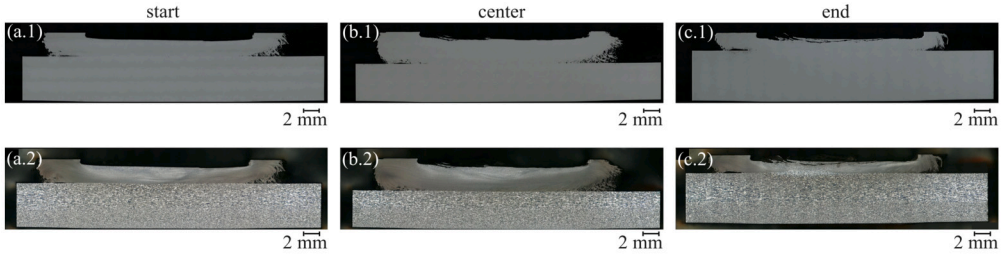

Fig. 9. Macrographs before and after etching for cross sections taken from AA2024 FS deposit with HFDB post-processing at (a) start, (b) center and (c) end along the groove, as presented in Fig. 1.

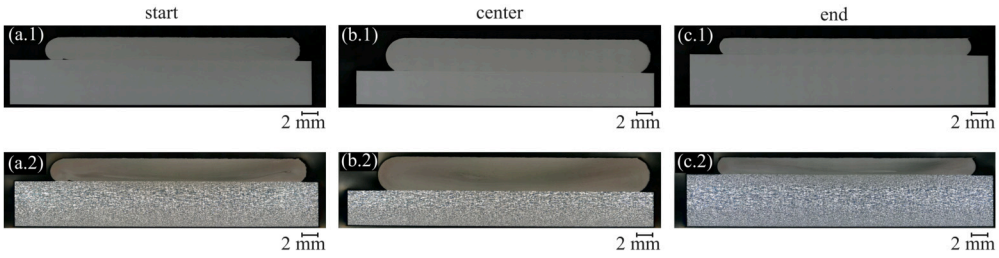

Fig. 10. Macrographs before and after etching for cross sections taken from AA2024 AFSD deposit at (a) start, (b) center and (c) end along the groove, as presented in Fig. 1.

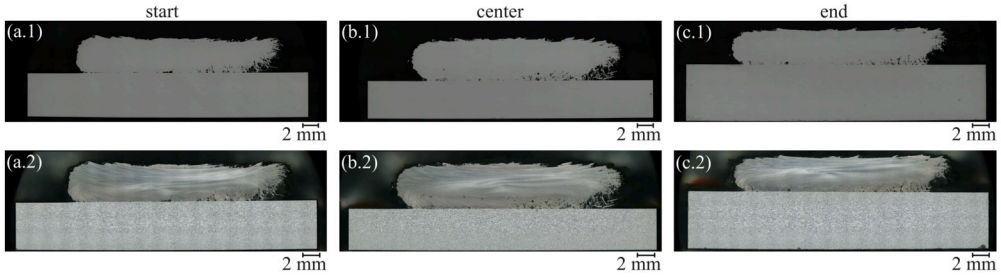

Fig. 11. Macrographs before and after etching for cross sections taken from AA7075 FS deposit at (a) start, (b) center and (c) end along the groove, as presented in Fig. 1.

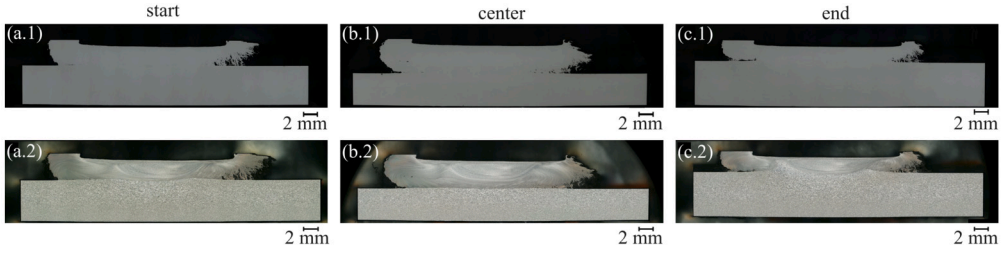

Fig. 12. Macrographs before and after etching for cross sections taken from AA7075 FS deposit with HFDB post-processing at (a) start, (b) center and (c) end along the groove, as presented in Fig. 1.

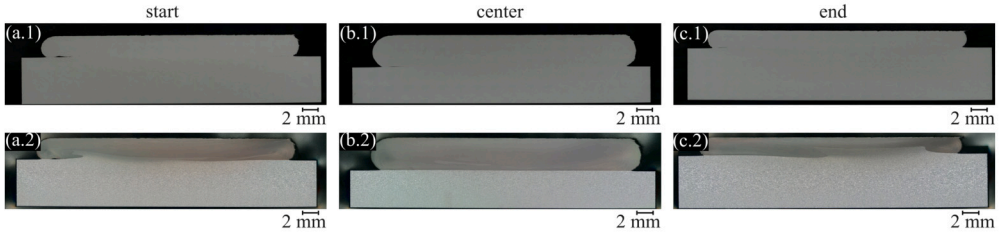

Fig. 13. Macrographs before and after etching for cross sections taken from AA7075 AFSD deposit at (a) start, (b) center and (c) end along the groove, as presented in Fig. 1.

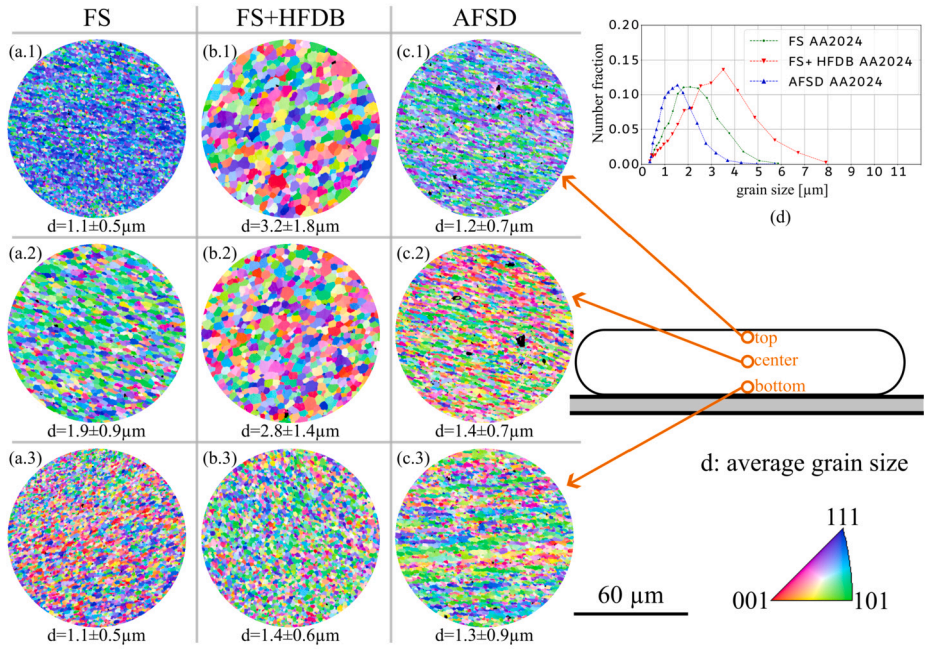

Fig. 14. Inverse pole figure (IPF) maps taken from cross sections at center of the groove for three positions along layer thickness, i.e., top, center and bottom, for friction surfacing (FS) (a.1-a.3), FS with hybrid friction diffusion bonding (FS+HFDB) (b.1-b.3) and additive friction stir deposition (AFSD) (c.1-c.3) using AA2024 consumable material. Particles and secondary phases lead to low confidence index regions below 0.2, resulting in black color in the IPF maps. The number fraction grain size distribution for the center EBSD scan position is shown in (d).

of FS with HFDB post-processing, presents a deeper heat-affected zone. Within the deposit, the FS and FS+HFDB samples present a hardness increase towards the top of the deposit, which is commonly known for FS layers of precipitation-hardenable aluminum alloys [13] and is a result of the local temperature distribution throughout the layer deposition process. The FS+HFDB sample presents a higher hardness than the FS sample in the center within the HFDB-processed (consolidated) area. Similar to FS, HFDB might lead to local solubilization of alloying elements and secondary phases. The top part cools down faster than the bottom due to convection and less overaging is assumed. The AA2024 AFSD sample presents a low and homogeneous hardness within the deposited material. As a result of the slower travel speed used in AFSD, the heat accumulated during the process takes longer to cool down, enabling the precipitates to grow and overage. The overaging phenomena are assumed to start just after the layer formation, as the θ (Al_2Cu) and S (Al_2CuMg) phase have a solidus temperature just below the process temperature, which is approximately 60-90% of the material's melting temperature for friction stir-based processes [49]. This causes a homogeneous low hardness value in the deposit. The AA7075 AFSD deposit, Fig. 16(f), presents the characteristic trend along deposit height with slightly higher hardness at the top [50]. Compared to the respective AA7075 FS and FS+HFDB deposits, Fig. 16(d, e), the hardness is significantly lower. Additionally, the minimum hardness within the substrate material is also lower than observed for the respective FS or FS+HFDB samples. Compared to AA2024 consumable material, the AA7075 AFSD deposit does not show a homogeneous drop of hardness, but a similar trend to the FS and FS+HFDB deposits. This occurs because the characteristic η ($MgZn_2$) precipitates feature a lower solidus temperature.[3] The temperature control during AFSD limited the temperature to 360° during deposition. However, the measuring thermocouple, is 1 mm away from the tool face. The localized temperature is likely to present higher temperatures due to the high shear rates near the tool face, which would promote partial or full dissolution of the precipitates. So, the precipitates solubilize during the process, and afterwards, during cooling, they precipitate and overage less, resulting in a higher hardness compared to 2xxx aluminum alloy series. Considering the substrates, AA7475 is expected to feature less stability to temperature than AA2024, meaning it suffers more overaging or solubilization of precipitates, hence the lower hardness in the area below the deposit.

Process temperatures (measured in the substrate) for FS of AA2024 can be expected to be around 400 °C [31], assuming that the groove geometry is similar to a flat surface. This is in agreement with process simulations of this material, see, for instance, [54,55]. Similar temperature ranges were reported in the experimental-numerical investigation

[3] The lowest solid solution temperature recommended by ASTM standard is 465 °C [51]. However, literature shows that also lower temperatures lead to the solubilization of η precipitates in the aluminum matrix, e.g., 440 °C for FS deposits [52], or even 400 °C for friction extruded wires [53].

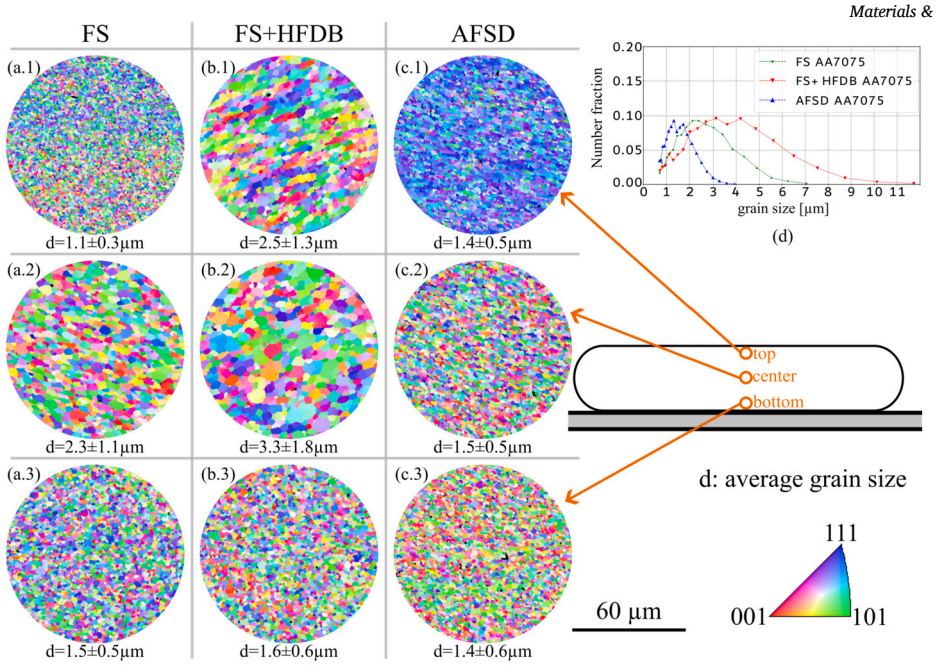

Fig. 15. Inverse pole figure (IPF) maps taken from cross sections at center of the groove for three positions along layer thickness, i.e., top, center and bottom, for friction surfacing (FS) (a.1-a.3), FS with hybrid friction diffusion bonding (FS+HFDB) (b.1-b.3) and additive friction stir deposition (AFSD) (c.1-c.3) using AA7075 consumable material. Particles and secondary phases lead to low confidence index regions below 0.2, resulting in black color in the IPF maps. The number fraction grain size distribution for the center EBSD scan position is shown in (d).

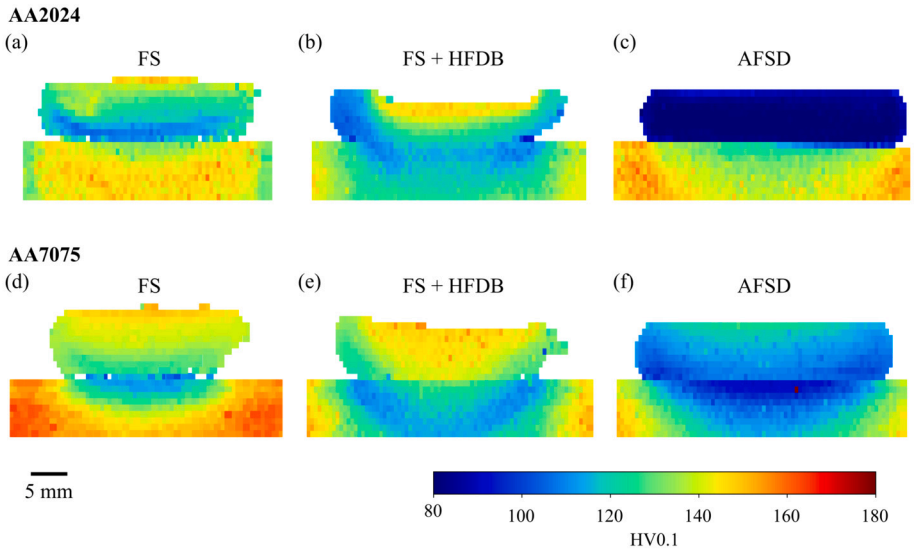

Fig. 16. Hardness distribution for cross section taken from the center of the groove for AA2024 (a-c) and AA7075 (d-f) consumable material via (a, d) FS, (b, e) FS with additional HFDB post-processing and (c, f) AFSD.

of multi-layer FS of AA7075 consumable material by Jadot et al. [56]. The AFSD process tends to reach higher process temperatures compared to FS because of the significant differences in terms of the heat dissipation conditions. As the shoulder is made from steel, the heat is stored and remains in the setup. The shoulder around the consumable material leads to heat accumulation after the process is initiated and the consumable material is continuously heating up, leading to higher maximum process temperatures compared to the FS process, where the heat is able to dissipate to the environment more easily.

The result obtained via the Imprintec indentation method, yield strength, $R_{p0.2}$, ultimate tensile strength, R_m and elongation, A, are presented in Table 4. For AA2024 consumable material, the yield strength for FS and FS+HFDB are both between 300 and 350 MPa. The FS+HFDB sample presented a higher ultimate tensile strength at lower elongation. This observation might be related to the changes in precipitate size and distribution as well as microstructure by the HFDB post-processing. The AFSD AA2024 deposit presents a lower yield and ultimate tensile strength, which is in agreement with the low hardness related to the dissolution and aging of precipitates. For AA7075 consumable material, the results in terms of $R_{p0.2}$, R_m and A for FS and FS+HFDB are similar, indicating that the additional HFDB post-processing cycles do not have a significant effect on properties obtained by this indentation method. Similar to the observations for AA2024, the AA7075 AFSD deposits also present a slightly lower strength compared to the other approaches, which is related to the process temperature and is in agreement with the results from the Vickers hardness measurements mentioned above.

Overall, for both alloys investigated, the AFSD deposits present a significantly lower hardness and strength, both obtained via indentation

Table 4
Average and one standard deviation for yield strength ($R_{p0.2}$), ultimate tensile strength (R_m) and elongation (A) obtained from Imprintec indentation method at the cross section taken from the center of the groove for AA2024 and AA7075 consumable material.

	AA2024			AA7075		
	FS	FS+HFDB	AFSD	FS	FS+HFDB	AFSD
$R_{p0.2}$ [MPa]	308.0 ± 5.1	334.0 ± 24.0	176.8 ± 6.3	367.5 ± 16.7	392.9 ± 16.8	298.3 ± 4.7
R_m [MPa]	383.4 ± 5.0	465.5 ± 54.2	266.6 ± 3.0	463.0 ± 9.9	473.7 ± 9.9	370.5 ± 2.9
A [%]	27.9 ± 2.3	21.9 ± 2.8	19.0 ± 1.2	21.2 ± 1.7	21.9 ± 2.5	29.3 ± 3.4

methods, compared to the approaches of FS and FS+HFDB. For that reason, groove repair via FS+HFDB might be preferable in a possible application considering the process setups and conditions presented in this work.

4. Conclusion

This study provides a direct comparison of FS and AFSD for a specific groove geometry for the first time. The process behavior as well as the respective deposits' characteristic, including an in-depth defect analysis and investigation of cross sections, is presented and discussed. For both approaches, a stable deposition behavior was achieved. The FS approach presented the most difficulties with regard to the bonding within the groove area; however, this can successfully be improved when HFDB is applied as post-processing technique. From a processing perspective, AFSD is advantageous because the layer thickness can be controlled and a successful groove repair could be achieved in one process run, whereas FS with HFDB needs multiple processing cycles via FS and HFDB, respectively. In contrast, the approach of FS+HFDB has lower requirements with regard to maximum axial force and torque during the layer deposition. Moreover, the deposits present a significantly higher hardness and a smaller heat-affected zone within the substrate material compared to the AFSD approach, using the process parameters and setup presented.

The work presents an insight into the effectiveness of different friction stir-based solid-state layer deposition approaches for the repair of a specific groove geometry. However, the effectiveness of the approaches is dependent on several aspects, like groove geometry and dimensions, materials or requirements with regard to the properties of the final repaired structure. The approaches investigated in this study, could be further improved, for instance, when a larger diameter of the HFDB tool is used to improve the effectiveness of the consolidation at the outer parts of the deposit. In terms of mechanical properties, a heat treatment of the repaired structure could be used to optimize the properties; however, this might lead to grain growth and the possibility of a heat treatment application might not be given for some application scenarios. The examples show that there are several factors, influencing the suitability of the (solid-state) processes. However, the presented work gives an insight into the strengths and weaknesses of different approaches and clearly further highlights the potential of friction stir-based techniques for this kind of applications. The next research steps in assessment and comparison of the solid state repair approaches need to contain more in depth mechanical testing, for instance, investigation of fatigue performance. In addition, it is necessary to investigate and compare the residual stress distribution and corrosion susceptibility to develop the approaches further towards application.

CRediT authorship contribution statement

Zina Kallien: Writing – review & editing, Writing – original draft, Visualization, Validation, Project administration, Methodology, Investigation, Formal analysis, Data curation, Conceptualization. **Victor A. Rojas:** Writing – review & editing, Visualization, Validation, Investigation, Formal analysis, Data curation. **Pietro Aspes:** Writing – review & editing, Visualization, Validation, Investigation, Formal analysis, Data curation. **Adam N. Swinney:** Writing – review & editing, Visualization, Validation, Investigation, Formal analysis, Data curation. **Trevor J. Fleck:** Writing – review & editing, Supervision, Resources, Funding acquisition. **J. Brian Jordon:** Writing – review & editing, Supervision, Resources, Funding acquisition. **Paul G. Allison:** Writing – review & editing, Supervision, Resources, Funding acquisition. **Benjamin Klusemann:** Writing – review & editing, Supervision, Resources, Funding acquisition.

Funding

Baylor University and the PONI Center acknowledge with gratitude the financial support of the US Department of Defense Strategic Environmental Research and Development Program, project number WP21-C4–1102.

The group of B.K. acknowledges funding from the European Research Council (ERC) under the European Unions Horizon 2020 research and innovation programme (Grant Agreement No. 101001567).

Declaration of competing interest

The authors declare that they have no known competing financial interests or personal relationships that could have appeared to influence the work reported in this paper.

Acknowledgements

The authors would like to extend thanks to the team at the PONI Center at Baylor University.

Appendix A. Supplementary material

Supplementary material related to this article can be found online at https://doi.org/10.1016/j.matdes.2025.114511.

Data availability

Part of this data is available online on Zenodo (DOI: 10.5281/zenodo.16792240). The remaining data is available on request.

References

[1] N. Tuncer, A. Bose, Solid-state metal additive manufacturing: a review, JOM 72 (9) (2020) 3090–3111, https://doi.org/10.1007/s11837-020-04260-y.
[2] O. Abdulhameed, A. Al-Ahmari, W. Ameen, S.H. Mian, Additive manufacturing: challenges, trends, and applications, Adv. Mech. Eng. 11 (2) (2019) 1687814018822880, https://doi.org/10.1177/1687814018822880.
[3] E. Cicală, G. Duffet, H. Andrzejewski, D. Grevey, S. Ignat, Hot cracking in Al-Mg-Si alloy laser welding - operating parameters and their effects, Mater. Sci. Eng. A 395 (1–2) (2005) 1–9, https://doi.org/10.1016/j.msea.2004.11.026.
[4] J. Bai, H. Ding, J. Gu, X. Wang, H. Qiu, Porosity Evolution in Additively Manufactured Aluminium Alloy During High Temperature Exposure, IOP Conf. Series: Mater. Sci. Eng., vol. 167, IOP Publishing, 2017, 012045.
[5] C. Li, Z. Liu, X. Fang, Y. Guo, Residual stress in metal additive manufacturing, Proc. CIRP 71 (2018) 348–353, https://doi.org/10.1016/j.procir.2018.05.039.
[6] W.E. Frazier, Metal additive manufacturing: a review, J. Mater. Eng. Perform. 23 (6) (2014) 1917–1928, https://doi.org/10.1007/s11665-014-0958-z.

[7] J. Gandra, H. Krohn, R.M. Miranda, P. Vilaça, L. Quintino, J.F. Dos Santos, Friction surfacing—a review, J. Mater. Process. Technol. 214 (5) (2014) 1062–1093, https://doi.org/10.1016/j.jmatprotec.2013.12.008.

[8] M. Korgancı, Y. Bozkurt, Recent developments in additive friction stir deposition (AFSD), J. Mater. Res. Technol. 30 (2024) 4572–4583, https://doi.org/10.1016/j.jmrt.2024.04.179.

[9] A. Mukhopadhyay, P. Saha, P.K. Singh, M. Verma, Development and analysis of a powder bed friction stir (PBFS) additive manufacturing process for aluminum alloys: a study on friction-stirring pitch (ω/v) and print location, Addit. Manuf. 72 (2023) 103618, https://doi.org/10.1016/j.addma.2023.103618.

[10] W. Lyu, Y. Shen, Y. Tang, K. Yang, Z. Zhou, C. Zhao, Y. Lu, X. Guo, Particle-based friction stir additive manufacturing of an al-mg-mn alloy, Addit. Manuf. 103 (2025) 104768, https://doi.org/10.1016/j.addma.2025.104768.

[11] H. Chen, X. Meng, J. Chen, Y. Xie, J. Wang, S. Sun, Y. Zhao, J. Li, L. Wan, Y. Huang, Wire-based friction stir additive manufacturing, Addit. Manuf. 70 (2023) 103557, https://doi.org/10.1016/j.addma.2023.103557.

[12] B. Chaudhary, N.K. Jain, J. Murugesan, D. Sathiaraj, Study of microstructure evolution and mechanical properties in friction stir based additive multi-layer manufacturing of Al 6061 alloy: effect of feedstock material form and heat treatment, Mater. Today Commun. 34 (2023) 105156, https://doi.org/10.1016/j.mtcomm.2022.105156.

[13] J. Gandra, D. Pereira, R.M. Miranda, R. Silva, P. Vilaça, Deposition of AA6082-T6 over AA2024-T3 by friction surfacing - mechanical and wear characterization, Surf. Coat. Technol. 223 (2013) 32–40, https://doi.org/10.1016/j.surfcoat.2013.02.023.

[14] M.E. Perry, H.A. Rauch, R.J. Griffiths, D. Garcia, J.M. Sietins, Y. Zhu, Y. Zhu, Z.Y. Hang, Tracing plastic deformation path and concurrent grain refinement during additive friction stir deposition, Materialia 18 (2021) 101159, https://doi.org/10.1016/j.mtla.2021.101159.

[15] M. Soujon, Z. Kallien, A. Roos, B. Zeller-Plumhoff, B. Klusemann, Fundamental study of multi-track friction surfacing deposits for dissimilar aluminum alloys with application to additive manufacturing, Mater. Des. 219 (5) (2022) 110786, https://doi.org/10.1016/j.matdes.2022.110786.

[16] N. Zhu, D.Z. Avery, B.A. Rutherford, B.J. Phillips, P.G. Allison, J.B. Jordon, L.N. Brewer, The effect of anodization on the mechanical properties of AA6061 produced by additive friction stir-deposition, Metals 11 (11) (2021) 1773, https://doi.org/10.3390/met11111773.

[17] R.S. Mishra, R.S. Haridas, P. Agrawal, Friction stir-based additive manufacturing, Sci. Technol. Weld. Join. 27 (3) (2022) 141–165, https://doi.org/10.1080/13621718.2022.2027663.

[18] H.Z. Yu, R.S. Mishra, Additive friction stir deposition: a deformation processing route to metal additive manufacturing, Mater. Res. Lett. 9 (2) (2021) 71–83, https://doi.org/10.1080/21663831.2020.1847211.

[19] Y. Yamashita, K. Fujita, Newly developed repairs on welded area of lwr stainless steel by friction surfacing: technical report, J. Nucl. Sci. Technol. 38 (10) (2001) 896–900, https://doi.org/10.1080/18811248.2001.9715112.

[20] R. Damodaram, P. Rai, S. Cyril Joseph Daniel, R. Bauri, D. Yadav, Friction surfacing: a tool for surface crack repair, Surf. Coat. Technol. 422 (2021) 127482, https://doi.org/10.1016/j.surfcoat.2021.127482.

[21] H. Agiwal, H. Yeom, K.A. Ross, K. Sridharan, F.E. Pfefferkorn, Leak-tight crack repair for 304l stainless steel using friction surfacing, J. Manuf. Process. 79 (2022) 532–543, https://doi.org/10.1016/j.jmapro.2022.05.004.

[22] H. Agiwal, H. Yeom, N. Pocquette, K. Sridharan, F.E. Pfefferkorn, Friction surfacing and cold spray deposition for surface crack repair in austenitic stainless steels, Mater. Today Commun. 33 (2022) 104692, https://doi.org/10.1016/j.mtcomm.2022.104692.

[23] L. Peter Martin, A. Luccitti, M. Walluk, Evaluation of additive friction stir deposition for the repair of cast Al-1.4 Si-1.1 Cu-1.5 Mg-2.1 Zn, J. Manuf. Sci. Eng. 144 (6) (2022) 061006, https://doi.org/10.1115/1.4052759.

[24] L.P. Martin, A. Luccitti, M. Walluk, Repair of aluminum 6061 plate by additive friction stir deposition, Int. J. Adv. Manuf. Technol. (2022) 1–15, https://doi.org/10.1007/s00170-021-07953-z.

[25] D.Z. Avery, C.E. Cleek, B.J. Phillips, M.Y. Rekha, R.P. Kinser, H.M. Rao, L.N. Brewer, P.G. Allison, J.B. Jordon, Evaluation of microstructure and mechanical properties of Al-Zn-Mg-Cu alloy repaired via additive friction stir deposition, J. Eng. Mater. Technol. 144 (3) (2022) 031003, https://doi.org/10.1115/1.4052816.

[26] R.J. Griffiths, D.T. Petersen, D. Garcia, H.Z. Yu, Additive friction stir-enabled solid-state additive manufacturing for the repair of 7075 aluminum alloy, Appl. Sci. 9 (17) (2019) 3486, https://doi.org/10.3390/app9173486.

[27] N. Zhu, T. Hickok, K.A. Fraser, D. Yu, Y. Chen, K. An, L.N. Brewer, P.G. Allison, J.B. Jordon, Neutron diffraction analysis of residual stress distribution in the lubricant-free TR-AFSD AA7075 repair coupled with SPH simulations, J. Adv. Join. Process. (2025) 100283, https://doi.org/10.1016/j.jajp.2025.100283.

[28] H. Wang, Y. Li, M. Zhang, W. Gong, R. Lai, Y. Li, Preheating-assisted solid-state friction stir repair of Al-Mg-Si alloy plate at different rotational speeds, Int. J. Miner. Metal. Mater. 31 (4) (2024) 725–736, https://doi.org/10.1007/s12613-023-2772-9.

[29] Z. Zhou, Y. Shen, W. Lyu, W. Xiong, Z. He, Y. Lin, Z. Zhou, X. Guo, Interface stair-like design and repair performance of Al-Zn-Mg-Cu aluminum alloy based on additive friction stir deposition, J. Mater. Process. Technol. (2025) 118758, https://doi.org/10.1016/j.jmatprotec.2025.118758.

[30] T. Köhler, M. Schiele, M. Glaser, K. Schricker, J. Bergmann, K. Augsburg, In-situ monitoring of hybrid friction diffusion bonded EN AW 1050/EN CW 004A lap joints using artificial neural nets, Proc. IME, Part L J. Mater. Des. Appl. 234 (5) (2020) 766–785, https://doi.org/10.1177/1464420720912773.

[31] M. Hoffmann, A. Roos, B. Klusemann, Investigation of microstructural and mechanical properties in AA2024-T351 multi-layer friction surfacing, Surf. Coat. Technol. 480 (2024) 130610, https://doi.org/10.1016/j.surfcoat.2024.130610.

[32] J. Li, M. Jadot, J. Xie, M.B. Lezaack, T. Sapanathan, R. Gautier, M. Rachik, A. Simar, Process parameters selection for multi-layer friction surfacing of 7075 aluminium alloy, Sci. Technol. Weld. Join. 29 (5–6) (2024) 328–336, https://doi.org/10.1177/13621718241275092.

[33] E. Yasa, O. Poyraz, K. Do, A. Molyneux, J. McManus, J. Hughes, In-situ monitoring and control of additive friction stir deposition, Materials 18 (7) (2025) 1509, https://doi.org/10.3390/ma18071509.

[34] G.R. Merritt, M.B. Williams, P.G. Allison, J.B. Jordon, T.W. Rushing, C.A. Cousin, Closed-loop temperature and force control of additive friction stir deposition, J. Manuf. Mater. Process. 6 (5) (2022) 92, https://doi.org/10.3390/jmmp6050092.

[35] J. Glenn, L. Dean, A. Wright, Y. Hovanski, Closed-loop PID temperature control of additive friction stir deposition, in: TMS Annual Meeting & Exhibition, 2023, pp. 15–25.

[36] P.G. Allison, J.B. Jordon, Friction based additive manufacturing systems and methods, 2023.

[37] N. Palya, K. Fraser, Y. Hong, N. Zhu, M. Williams, K. Doherty, P. Allison, J. Jordon, Multi-physics approach to predict fatigue behavior of high strength aluminum alloy repaired via additive friction stir deposition, Integr. Mater. Manuf. Innov. 12 (4) (2023) 441–455, https://doi.org/10.1007/s40192-023-00309-3.

[38] G. Chen, K. Wu, Y. Wang, Y. Sun, X. Wang, Z. Zhu, F. Hu, Quantitative study on the correlation between microstructure and mechanical properties of additive friction stir deposited 6061-t6 al-mg-si alloy, J. Mater. Res. Technol. 25 (2023) 6725–6736, https://doi.org/10.1016/j.jmrt.2023.07.097.

[39] S. Ding, S.A. Khan, J. Yanagimoto, Metadynamic recrystallization behavior of 5083 aluminum alloy under double-pass compression and stress relaxation tests, Mater. Sci. Eng. A 822 (2021) 141673.

[40] DIN SPEC 4864, Prüfverfahren zur Ermittlung von Fließkurven und Vergleichskennwerten zum Zugversuch Mittels Zerstörungsarmem Prüfeindruck, 3D-Vermessung und Finitelemente Werkstoffmodell, 2019.

[41] B. Schmaling, A. Hartmaier, Determination of plastic material properties by analysis of residual imprint geometry of indentation, J. Mater. Res. 27 (16) (2012) 2167–2177, https://doi.org/10.1557/jmr.2012.212.

[42] J. Gandra, R.M. Miranda, P. Vilaça, Performance analysis of friction surfacing, J. Mater. Process. Technol. 212 (8) (2012) 1676–1686, https://doi.org/10.1016/j.jmatprotec.2012.03.013.

[43] N. Gotawala, H.Z. Yu, Material flow path and extreme thermomechanical processing history during additive friction stir deposition, J. Manuf. Process. 101 (2023) 114–127, https://doi.org/10.1016/j.jmapro.2023.05.095.

[44] Z. Kallien, M. Hoffmann, A. Roos, B. Klusemann, Correlation of microstructure and local mechanical properties along build direction for multi-layer friction surfacing of aluminum alloys, JOM 75 (2023) 4212–4222, https://doi.org/10.1007/s11837-023-06046-4.

[45] M. Hoffmann, Z. Kallien, E.A. Duda, B. Klusemann, Insight into layer formation during friction surfacing: relationship between deposition behavior and microstructure, Mater. Today Commun. 41 (2024) 110337, https://doi.org/10.1016/j.mtcomm.2024.110337.

[46] W. Tang, X. Yang, C. Tian, Y. Xu, Microstructural heterogeneity and bonding strength of planar interface formed in additive manufacturing of Al- Mg- Si alloy based on friction and extrusion, Int. J. Miner. Metal. Mater. 29 (9) (2022) 1755–1769, https://doi.org/10.1007/s12613-022-2506-4.

[47] M.M. El-Rayes, E.A. El-Danaf, The influence of multi-pass friction stir processing on the microstructural and mechanical properties of aluminum alloy 6082, J. Mater. Process. Technol. 212 (5) (2012) 1157–1168, https://doi.org/10.1016/j.jmatprotec.2011.12.017.

[48] A. Heidarzadeh, S. Mironov, R. Kaibyshev, G. Çam, A. Simar, A. Gerlich, F. Khodabakhshi, A. Mostafaei, D.P. Field, J.D. Robson, A. Deschamps, P.J. Withers, Friction stir welding/processing of metals and alloys: a comprehensive review on microstructural evolution, Prog. Mater. Sci. 117 (2021) 100752, https://doi.org/10.1016/j.pmatsci.2020.100752.

[49] R. Mishra, Z. Ma, Friction stir welding and processing, Mater. Sci. Eng., R Rep. 50 (1) (2005) 1–78, https://doi.org/10.1016/j.mser.2005.07.001.

[50] F. Girault, L. Toualbi, Q. Barres, E. Charkaluk, Investigating multi-scale heterogeneity in multi-layer additive friction stir deposition of high-strength aluminum alloys, Mater. Sci. Eng. A 927 (2025) 147979, https://doi.org/10.1016/j.msea.2025.147979.

[51] B07 Committee, Practice for Heat Treatment of Wrought Aluminum Alloys, https://doi.org/10.1520/B0918_B0918M-20A.

[52] P. Liu, F.C. Liu, Y.D. Wang, Z. Zhang, P. Xue, L.H. Wu, H. Zhang, D.R. Ni, B.L. Xiao, Z.Y. Ma, Additive manufacturing of commercial Al–Zn–Mg–Cu aluminum alloys with mechanical properties comparable to extruded counterparts, Mater. Sci. Eng. A 899 (2024) 146441, https://doi.org/10.1016/j.msea.2024.146441.

[53] R. Kalsar, X. Ma, J. Darsell, D. Zhang, K. Kappagantula, D.R. Herling, V.V. Joshi, Microstructure evolution, enhanced aging kinetics, and mechanical properties of AA7075 alloy after friction extrusion, Mater. Sci. Eng. A 833 (2022) 142575, https://doi.org/10.1016/j.msea.2021.142575.

[54] H. Jamshidi Aval, Comprehensive thermo-mechanical simulation of friction surfacing of aluminum alloys using smoothed particle hydrodynamics method, Surf. Coat. Technol. 419 (2021) 127274, https://doi.org/10.1016/j.surfcoat.2021.127274.

[55] Z. Rahmati, H. Jamshidi Aval, S. Nourouzi, R. Jamaati, Modeling and experimental study of friction surfacing of AA2024 alloy over AA1050 plates, Mater. Res. Express 6 (8) (2019), https://doi.org/10.1088/2053-1591/ab255a.

[56] M. Jadot, J. Li, R. Gautier, J. Xie, M.B. Lezaack, T. Sapanathan, M. Rachik, A. Simar, Analysis of grain structure, precipitation and hardness heterogeneities, supported by a thermal model, for an aluminium alloy 7075 deposited by solid-state multi-layer friction surfacing, J. Mater. Process. Technol. 335 (2025) 118661, https://doi.org/10.1016/j.jmatprotec.2024.118661.